A processing chain for estimating crop biophysical parameters using temporal Sentinel-1 synthetic aperture radar data in cloud computing framework

Mandal, Dipankar; Kumar, Vineet; Lopez-Sanchez, Juan M.; Rao, Y. S.; McNairn, Heather; Bhattacharya, Avik; Mitchell, Scott

DOI
10.1016/B978-0-12-823457-0.00011-2

Publication date
2022

Document Version
Final published version

Published in
Radar Remote Sensing

Citation (APA)
Mandal, D., Kumar, V., Lopez-Sanchez, J. M., Rao, Y. S., McNairn, H., Bhattacharya, A., & Mitchell, S. (2022). A processing chain for estimating crop biophysical parameters using temporal Sentinel-1 synthetic aperture radar data in cloud computing framework. In *Radar Remote Sensing: Applications and Challenges* (pp. 309-325). Elsevier. https://doi.org/10.1016/B978-0-12-823457-0.00011-2

CHAPTER 16

A processing chain for estimating crop biophysical parameters using temporal Sentinel-1 synthetic aperture radar data in cloud computing framework

Dipankar Mandal[1,2], Vineet Kumar[3], Juan M. Lopez-Sanchez[4], Y.S. Rao[1], Heather McNairn[5], Avik Bhattacharya[1] and Scott Mitchell[6]

[1]Microwave Remote Sensing Lab, Centre of Studies in Resources Engineering, Indian Institute of Technology Bombay, Mumbai, Maharashtra, India; [2]Department of Agronomy, Kansas State University, Manhattan, KS, United States; [3]Department of Water Resources, Delft University of Technology, Delft, the Netherlands; [4]Institute for Computer Research, University of Alicante, Alicante, Spain; [5]Ottawa Research and Development Centre, Agriculture and Agri-Food Canada, Ottawa, ON, Canada; [6]Geomatics and Landscape Ecology Laboratory, Carleton University, Ottawa, ON, Canada

1. Introduction

Operational crop growth monitoring is necessary to realize yield forecasts and map inventories at a local and regional level. To achieve such objects, certain countries have engaged with several operational groups to develop monitoring systems including Monitoring Agricultural Resources (MARS) (Baruth et al., 2008), Forecasting Agricultural output using Space (FASAL) (Parihar et al., 2006), CropWatch (Wu et al., 2014), and Integrated Canadian Crop Yield Forecaster (ICCYF) (Chipanshi et al., 2015). These crop monitoring systems function within a growing period through the collection of timely information on plant conditions, meteorologic data, and yield expectations. Complementary synoptic information about spatiotemporal variations in crop growth and phenology stages can be provided using satellite imagery. With decades of investigation and advancement, researchers well-instituted and advocated an operational crop monitoring and yield forecasting framework in the optical regime (Mulla et al., 2013; Khamala et al., 2017; Fritz et al., 2019; deFourny et al., 2019). These frameworks frequently derive either measurable growth indicators (e.g., leaf area index [LAI], plant water content, chlorophyll absorption) or vegetation indices (e.g., normalized difference vegetation index, enhanced vegetation index) as by-products.

Operational frameworks that rely on satellite data from optical sensors are restricted to data acquisition under clear sky states. A cloudy scene may keep a continuous time series from being achieved for crop development. On the contrary, synthetic aperture radar (SAR) measurements are seldom affected by sky conditions including cloud cover. Indeed, it has gained attention for agricultural applications because of the sensitivity of the microwave signal to dielectric and geometrical characteristics of the target. However, radar

Radar Remote Sensing
ISBN 978-0-12-823457-0, https://doi.org/10.1016/B978-0-12-823457-0.00011-2

backscatter coefficients or other secondary parameters (such as scattering power decomposition parameters) (Cloude et al., 1996) cannot be used directly in existing optical-driven models.

A reasonable trail can be followed by obtaining similar vegetation metrics (e.g., LAI or biomass) from SAR measurements. These metrics have been generated from optical sensors as operational products (e.g., Moderate Resolution Imaging Spectroradiometer (MODIS) vegetation products). We can achieve better yield estimates from agricultural monitoring frameworks by assimilating SAR data-derived crop biophysical parameters along with phenological developments. Such intense measurements have become possible with accelerated efforts by several space agencies to expand the constellations of satellites by commissioning the Sentinel-1 series, Satélite Argentino de Observación COn Microondas (SAOCOM), Radarsat Constellation Mission (RCM), and the upcoming NASA-ISRO Synthetic Aperture Radar (NISAR) and Radar Observing System for Europe - L-Band (ROSE-L). The individual observation covers a wide swath, which would facilitate the production of within-season crop inventories with reasonable accuracy.

In the SAR literature, the semiempirical water cloud model (WCM) (Attema and Ulaby, 1978) is recognized for realizing SAR scattering phenomena within vegetation targets owing to its relative simplicity and inversion for these vegetation descriptors (Graham, 2003; Steele-Dunne et al., 2017). Several studies have been undertaken to estimate biophysical parameters from SAR data for different crops (Lievens et al., 2011; Prevot et al., 1993; Chakraborty et al., 2005; Dabrowska et al., 2007; Inoue et al., 2014; Beriaux et al., 2015; Hosseini et al., 2015, 2017; Mattia et al., 2015; Fieuzal et al., 2016; Mandal et al., 2021). Although these experiments are specific to crop and test sites, it recommends feasible schemes to invert the WCM to retrieve crop biophysical variables with adequate accuracy and scalability.

Nevertheless, an estimation of biophysical parameters via the WCM inversion scheme may lead to an ill-posed problem. Such cases have been potentially addressed with the iterative optimization (IO) and lookup table (LUT) search techniques (Prevot et al., 1993; Mandal et al., 2021). However, the traditional methods impartially deliver realistic estimations at the expense of high computational support when optimizing such inversion problems (Mandal et al., 2019a). Recognizing the inherent concerns with conventional methods (IO and LUT search) for deployment at larger scales, ill-posed inversion problems are customarily solved by data-driven nonparametric models to produce a stable and optimum solution (Beriaux et al., 2011; Verrelst et al., 2012; Mandal et al., 2019b). In a cross-site experiment setting, Mandal et al. (2019a) reported the superiority of machine learning regression approaches compared with traditional ones for the inversion of WCM in terms of accuracy and efficient computation time. Data-driven nonparametric models in the machine learning regression family can provide a proper method for WCM inversion in operational applications (Chauhan et al., 2018; Mandal et al., 2019a).

Operational crop monitoring benefits from Earth observation (EO) data with high temporal revisit and extended spatial coverage. In this context, open data through the C-band Sentinel-1 SAR constellation mission adheres to EO specifications for global

agricultural monitoring (Whitcraft et al., 2019). It has become important to evaluate model inversion methodologies to test their accuracy for operational use (GEOGLAM, 2012). Nevertheless, the dense acquisition of Sentinel-1 data created several challenges in operational employment in terms of the data volume and the requirements of computational infrastructure (Wagner, 2015; Ali et al., 2017). To build efficient platforms for regional-scale mapping, efforts have been made by different space agencies by inducting the enactment of commercial cloud computing platforms. For instance, Sentinel-1 data are open on Google Earth Engine (GEE) clouds as well as Amazon Web Services. Similarly, for the upcoming NISAR mission, the Alaska Satellite Facility Distributed Active Archive Centers (DAAC) is exploring a preliminary prototype of a cloud-based system (NISAR Science Team, 2018). This approach is currently being tested with Sentinel-1 (approximately 5 GB of data volume per frame) as a surrogate for NISAR data (approximately 25 GB per frame).

The GEE enables users to fetch and process Sentinel-1 data instantly on the cloud platform as an alternative to downloading and processing in a local workstation (Gorelick et al., 2017). Several studies showcased the utility of GEE and the efficiency of custom-built processing pipelines for crop classification and mapping (Torbick et al., 2017; Xiong et al., 2017; Shelestov et al., 2017; Mandal et al., 2018), LAI products from MODIS data (Campos et al., 2018), and crop production evaluation (Lobell et al., 2015). However, Sentinel-1 data have not been fully explored in GEE for the delivery of crop inventories.

The overarching goal of the investigation is to appraise the potential and transferability of the model inversion method from a point to a regional scale with Sentinel-1 data in a GEE processing chain. In this chapter, we introduce a comprehensive evolution of a processing chain, GEE4Bio, in a cloud platform to estimate crop biophysical variables using Sentinel-1 products. Apart from the inventory map generation, coupling the Google Colab with the GEE permits us to achieve WCM calibration for individual crops and to assess the retrieval accuracies. The inversion of WCM is implemented into the GEE platform. Instead of a traditional LUT search and iterative approaches, the Random Forest (RF) regression is used as the inversion approach to retrieve the plant area index (PAI) and wet biomass using information from both the co- and cross-pol (VV-VH) channels of Sentinel-1. Furthermore, PAI and wet biomass maps for different crop growth stages are generated in the same processing chain.

2. Methodology

2.1 Study area and dataset

We conducted this investigation over the Joint Experiment for Crop Assessment and Monitoring (JECAM) test site for SAR Inter-Comparison Experiment in Carman, Manitoba (Canada), as given in Fig. 16.1. The Carman test site includes $\approx 26 \times 48\ km^2$ of the area and is designated by diverse agricultural crop types and soil conditions. Among several crop types, wheat, oats, soybean, canola, and corn are mostly

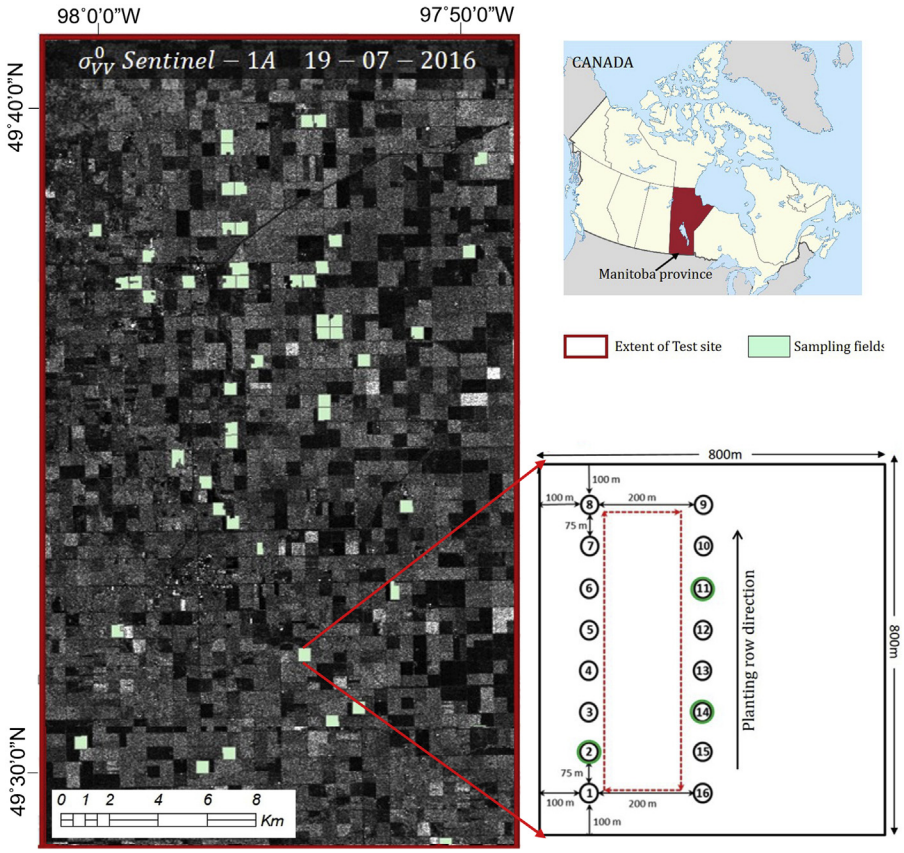

Figure 16.1 Study area over the Joint Experiment for Crop Assessment and Monitoring—Carman test site in Canada. The sampling fields (mint green polygons) are overlayed on the σ°_{VV} Sentinel-1 image acquired on Jul. 19, 2016. A layout of 16 sampling locations within a sampling field is highlighted.

grown during the summer. Ground data were collected nearly simultaneously with satellite overpasses during the SMAPVEX16-MB campaign in 2016 (Bhuiyan et al., 2018).

Throughout the SMAPVEX16-MB campaign, crop and soil in situ data from 50 fields were measured in two definite periods (i.e., June 8—22 and July 8—22, 2016). During this campaign window, measurements in most crop fields showed plant growth from an early to a fully vegetative stage. The nominal size of each field was approximately 800 m × 800 m. In each sampling field, soil moisture data were gathered from 16 sampling locations, arranged in two parallel transects along the row direction, as shown in Fig. 16.1. Soil moisture measurements were taken at these locations with three replicate measurements using Steven's Hydra Probes during both periods of the campaign (Bhuiyan et al., 2018). Among these 16 sampling locations, three were selected for vegetation sampling. In each sampling site, plant biomass (dry and wet), PAI

($m^2\ m^{-2}$), and crop phenological stages were recorded by destructive and nondestructive methods. On the contrary, PAI measurements were estimated using digital hemispherical photography and postprocessing images in CANEYE software. A detailed description of the test site and in situ measurement protocols can be found in SMAPVEX16-MB campaign reports (McNairn et al., 2016). We also used the annual crop inventory map developed by Agriculture and Agri-Food Canada (Davidson et al., 2017), which is open in the GEE Data Catalog. We used three Sentinel-1 acquisitions for this research, as listed in Table 16.1.

The preprocessing of these Sentinel-1 measurements to produce SAR backscatter intensities for each sampling location is described in detail in Section 2.2. Extracted backscatter intensities $\overset{\circ}{\sigma}_{VV}$ and $\overset{\circ}{\sigma}_{VH}$ are enumerated with corresponding in situ measurements for each acquisition date. These tabulated datasets are subsequently employed to calibrate and validate the WCM. From this entire feature set, the calibration data split is performed by selecting approximately half of the data randomly; the remainder of the data are used as an independent validation dataset for each individual crop. The first dataset is used in the WCM calibration, and the other for validation to evaluate the performance of the inversion method.

2.2 GEE4Bio: Sentinel-1 data processing chain in Google Earth Engine for biophysical parameter estimation

The processing chain involves two elemental segments considering the cloud computing environments within a unified framework: Earth Engine mode and Google Colab. Processing steps counted on Google Colab (Hoyos et al., 2006) are the calibration of WCM, creation of the LUT, and validation of inversion for each crop type. The inversion of the WCM and the generation of biophysical inventory maps are implemented on the GEE cloud platform.

The GEE can seamlessly manage the processing steps from time series of Sentinel-1 data fetching to model inversion. It typically encompasses five actions: (1) Sentinel-1 data fetching, (2) cloud filtering, (3) image preprocessing, (4) vegetation modeling and

Table 16.1 Sentinel-1 acquisitions and in situ measurement dates during the campaign.

Sentinel-1 image acquisition date	Beam mode	Incidence angle range	Orbit	In situ measurement dates
June 13, 2016	IW	31.32–35.24	Ascending	June 13, June 15
July 7, 2016	IW	31.32–35.24	Ascending	Jul. 5, July 6
July 19, 2016	IW	30.23–34.84	Ascending	Jul. 17, July 20

IW, interferometric wide swath mode.

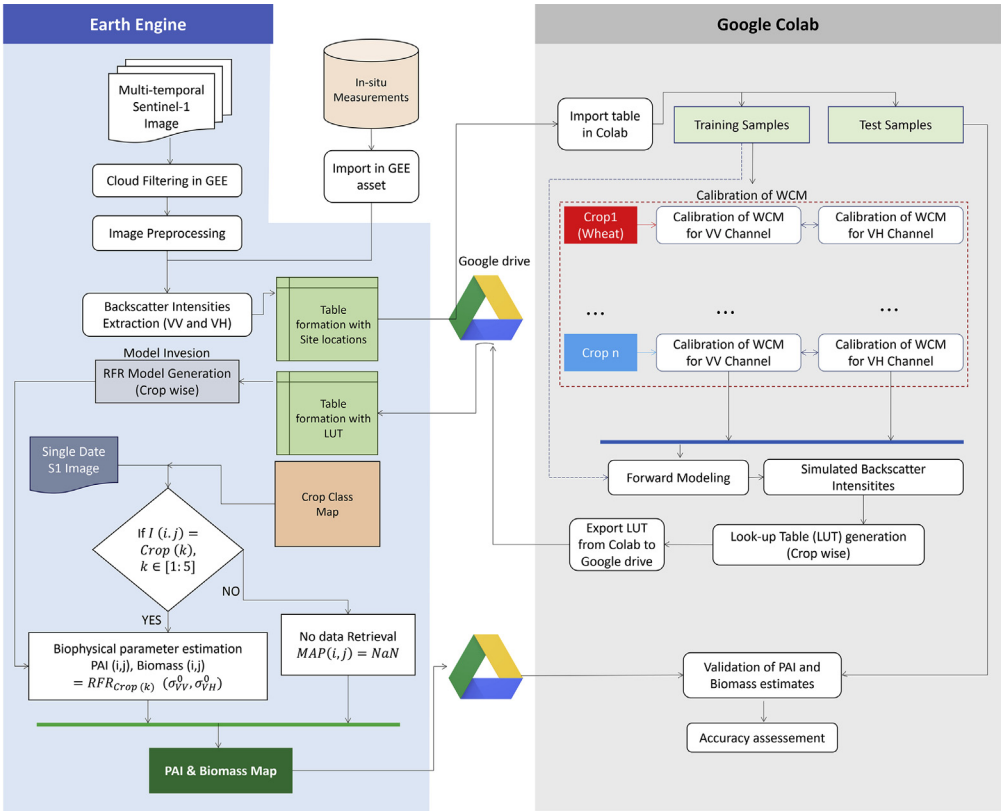

Figure 16.2 Schematic workflow of GEE4Bio processing chain for plant area index (PAI) and wet biomass retrieval. *GEE*, Google Earth Engine; *PAI*, plant area index; *RFR*, Random Forest regression; *WCM*, water cloud model.

calibration, and (5) model inversion and crop biophysical parameter map generation. The schematic workflow of the GEE4Bio processing chain for biophysical parameter estimation is presented in Fig. 16.2.

2.2.1 Sentinel-1 data fetching

We fetched the Sentinel-1A Ground Range Detected (GRD) products in the GEE processing Web application interface directly from the GEE Image collection. The image collection in GEE contains the calibrated and ortho-corrected products, which are preprocessed from the Single Look Complex data using the Sentinel-1 Toolbox (ESA, 2015).

2.2.2 Cloud filtering

The GEE image collection of Sentinel-1 data contains multiple metadata attributes regarding imaging properties including orbit pass type (ascending or descending),

acquisition mode (IW, etc.), and polarization. In the cloud filtering step, we select required images from the GEE image collection using associated attributes by employing the Metadata filtering function. Subsequently, spatial subsetting is performed followed by sorting images by date of acquisition using the filterDate argument.

2.2.3 Image preprocessing

The GEE image collection products of Sentinel-1 backscatter intensities are represented in dB scale. Hence, for further processing, we converted the data products to natural power scale by employing $10^{I_{ij}/10}$ conversion. Afterward, a 3×3 boxcar averaging sliding window filter is employed to degrade the speckle effect. The type and window size of the filter are determined according to the high field sizes and homogeneous cropping pattern (Robertson et al., 2018). The locations of in situ measurements are overlayed on these backscatter intensity images and σ° values are extracted both in VV and VH channels.

2.2.4 Vegetation modeling and calibration

The WCM enables the simulation of radar backscatter intensities from the vegetation–soil system using semiempirical models (Attema and Ulaby, 1978). The form of WCM adapted for backscatter calculations is (Eq. 16.1):

$$\sigma^{\circ} = AV_1^E \cos\theta\left(1 - \exp\left(-\frac{2BV_2}{\cos\theta}\right)\right) + D\exp(CM_v) \times \exp\left(-\frac{2BV_2}{\cos\theta}\right)\cos\theta \tag{16.1}$$

The vegetation descriptors are presented as $V_1 = \mathrm{L}$ and $V_2 = \mathrm{W}$, where L and W are the PAI and wet biomass, respectively. The WCM parameters (A, B, C, D, and E) are calibrated for each crop type individually in the Google Colab Web platform. The model parameters are determined using the nonlinear least square optimization employing the Levenberg–Marquardt algorithm (More, 1978). The WCM is calibrated for both co- and cross-pols for all crops employing the same in situ measurements. The model calibration realizations are evaluated in terms of the correlation coefficient (r) and root mean square error (RMSE) with the WCM simulated σ° and observed σ°.

2.2.5 Model inversion and crop biophysical parameter map generation

After calibration of the WCM, we determine the PAI and wet biomass by inverting the WCM. We employ a regression-based method to solve the ill-posed inversion case. The model inversion chain encompasses three principal actions: (1) WCM forward modeling and LUT generation, (2) regression model development, and (3) derivation of PAI and wet biomass maps.

The forward modeling denotes the generation of response values from an augmented dataset employed to train the regression model. We use the aggregates of crop descriptors from the calibration data in forward WCM to produce the corresponding σ° to form the LUT. In the Google Colab platform, a LUT is created using these vegetation parameters and the corresponding σ° for individual crop types. These LUTs are then put in tables independently for each crop.

The LUT elements are then employed as training data to constitute the RF regression (RFR) model in the GEE cloud. Radar data derived σ° in both the co-pol and cross-pol channels are introduced as RFR predictors. On the opposite side, the PAI and wet biomass measurements are employed as RFR targets. The formulation of RFR is well-established in machine learning theories, which often indicate RF as an ensemble learning technique (Breiman, 2001). It uses a large set of independently produced decision trees from the given training datasets. To build each tree, a random bootstrap sampling is conducted, which comprises 67% of the training samples. The remaining 33% of the training sample (often defined as out-of-bag [OOB] samples) is employed to get an error estimate for this subset. After building such multiple decision trees, the prediction is made by averaging the results of all trees, which can provide more accurate and stable predictions than individual decision trees. Another key concept of RF is the selection of random subsets of predictor features for node splitting. At each node, the best split is chosen to form the succeeding child nodes. The numerical value of each child node is taken as the mean of samples in that node (Liaw and Wiener, 2002). In this work, based on the OOB error rate, 300 trees are considered for RF regression, and the node impurity is measured with the mean square error.

During the inversion step, the PAI and wet biomass values are estimated using the RFR model trained by the LUT elements for each crop. Afterward, PAI and wet biomass inventory maps are generated over the test area in GEE using Sentinel-1 acquisitions and the annual crop class map.

3. Results and discussion

3.1 Water cloud model calibration

The calibration of the WCM is performed for VV and VH polarizations as previously discussed in Section 2.2.4 for the wheat, soybean, canola, corn, and oat crops. This step results in 10 different equations. The model parameters (i.e., A, B, C, D, E, and F) for each combination of crop and polarization are estimated along with the significance test analysis (F statistics and *P* values).

P values for all WCMs are <0.05, indicating a good fit for the dataset. Before forward modeling and LUT generation, the goodness of fit of calibrated WCM is assessed using the calibration dataset for each crop type. Backscatter intensities are simulated for the

Table 16.2 Error estimates of simulated and observed backscatter (σ°) for calibration data.

	VV		VH	
Crop	**r**	**Root mean square error**	**r**	**Root mean square error**
Wheat	0.80	0.026	0.62	0.007
Soybean	0.64	0.034	0.68	0.006
Canola	0.87	0.051	0.83	0.010
Oats	0.86	0.036	0.62	0.004
Corn	0.66	0.026	0.79	0.006

calibration dataset using the model parameters estimated for both VV and VH polarizations and individual crops, and the model accuracies are given in Table 16.2.

The correlation coefficients (r) in Table 16.2 confirm that the VV polarization is better calibrated for wheat, oats, and canola than VH polarization. The higher errors for soybean and corn canopies are likely a function of their more random (less vertical) canopy structures. Evidence of this lies in the comparatively lower errors for VH relative to VV polarizations for all of these crops.

3.2 Water cloud model inversion and validation

WCM inversion is achieved with VV and VH backscatter intensities from the validation dataset, as predictors in the RFR model. The accuracy of crop biophysical parameter estimates is assessed on a 1:1 plot against corresponding in situ measurements. Results are shown in Figs. 16.3 and 16.4 for all individual crops. Validation samples from three acquisition dates are presented in the 1:1 plot with cyan, green, and red dots, respectively.

3.2.1 Validation of plant area index

The estimated and ground measured PAIs for all five crops are presented in Fig. 16.3. The correlative plots for wheat indicated a high value of $r = 0.83$ between estimated and measured PAIs with an RMSE of 1.75 $m^2\ m^{-2}$. For wheat fields, the ground measured PAI ranges from 0.75 to 8.90 $m^2\ m^{-2}$ as plants advanced from leaf development to the fruiting stages. Estimates from the first acquisition (of Sentinel-1) follow the 1:1 line well. However, PAI values indicate an underestimation when wheat PAI is greater than 6.0 $m^2\ m^{-2}$ through the end of the heading stage. During this phenologic stage, PAI does not change with further wheat development. Rather, radar backscatter is governed by scattering from wheat heads (Mcnairn et al., 2004). The saturation of PAI estimates during the second, and third acquisitions is apparent in Fig. 16.3.

For soybean, the measured PAI varies from 0.2 to 4.6 $m^2\ m^{-2}$ with development during the SMAPVEX-16 campaign comprising growth stages from leaf development through flowering. The estimated and observed PAIs follow the 1:1 line well during these development stages, providing a correlation coefficient and RMSE of 0.91 and

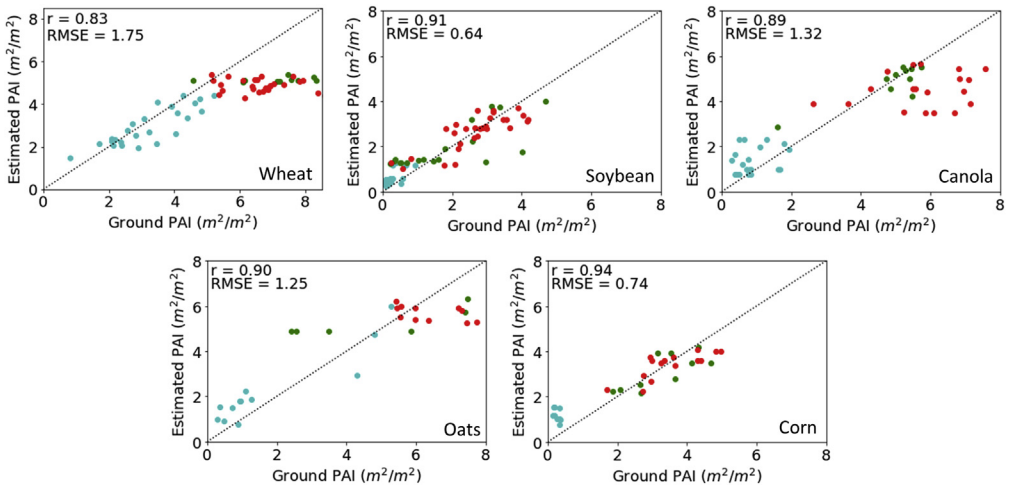

Figure 16.3 Validation plot of plant area index (PAI) ($m^2\ m^{-2}$) for each crop. Validation samples from three acquisition dates (i.e., June 13, July 7, and July 19) are presented in a 1:1 plot with cyan, green, and red, respectively. *RMSE*, root mean square error.

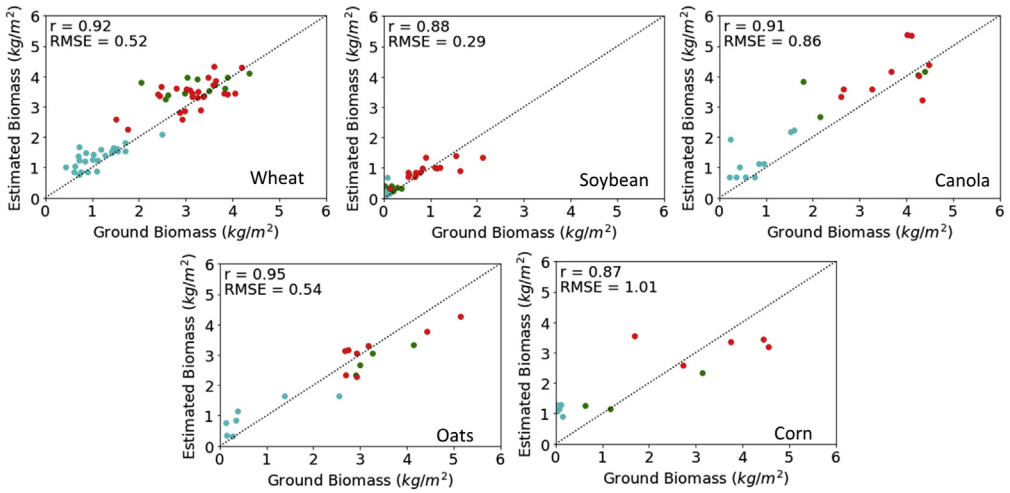

Figure 16.4 Validation plot of wet biomass ($kg\ m^{-2}$) for each crop. Validation samples from three acquisition dates (i.e., June 13, July 7, and July 19) are presented in a 1:1 plot with cyan, green, and red, respectively. *RMSE*, root mean square error.

0.64 $m^2\ m^{-2}$, respectively. Nonetheless, a greater spread (1.2 $m^2\ m^{-2}$) is noted for high PAI values when the soybean canopy closes at the end of side shoot formation. These disparities in PAI estimations may result from the differences in plant density in certain soybean fields. From the in situ measurements, we note that the number of plants along the row was higher for some fields (50 plants/m) relative to other fields (12 plants/m).

PAI assessments of canola (Fig. 16.3) indicate higher errors (RMSE of 1.32 $m^2\ m^{-2}$) relative to soybean, even though the correlation is significant ($r = 0.89$). During the early vegetative growth stage of canola, an overestimation in PAI can be observed, potentially explained by the dominant response from the underlying soil. Soil moisture and surface roughness have important roles during the early stage of crop development. However, in situ surface roughness measurements reported low surface roughness (average root mean square height and correlation length of 1.1 and 8.5 cm, respectively) over the sampling fields. Alternatively, soil moisture values deviate owing to disparity in soil texture in several fields (Bhuiyan et al., 2018), which might cause variations in backscatter intensities. With the advancement of canola to inflorescence emergence and flowering, an underestimation is apparent with PAI estimates. This underestimation at this period (PAI $>5.3\ m^2\ m^{-2}$) is likely due to saturation of the C-band (5.6 cm wavelength) wave with a high accumulation of plant biomass throughout the flowering and podding stage of canola.

The validation outcomes for oats show that although variations in terms of accuracy ($r = 0.90$ and RMSE $= 1.25\ m^2\ m^{-2}$) are modest compared with wheat, some differences over the 1:1 line are apparent. These agreements in results are likely due to higher similarities in the structures of these two cereal crop types. As with wheat, oats exhibit an erectophile leaf geometry during the early tillering phase. However, a difference is observed during the period of plant inflorescence when oat heads emerge. Unlike the formation of spikelets, as occurs during the inflorescence of wheat, oat plants form panicles during inflorescence. These panicles are attached to the central axis via branches and mantled by large paper-like covers (glumes), which contain two to three florets (Bleiholder, 2001). Thus, separation between these two crops with second acquisition estimates might be possible, as observed in Fig. 16.3. An underestimation is apparent during the third acquisition period when fruit development starts. During this period, PAI and biomass trends seldom increase proportionately for cereal crops.

As observed in Fig. 16.3, the PAI estimates of corn obey the 1:1 line reasonably well for the entire period of corn growth starting from leaf development to tasseling. The in situ measurement of PAI ranges from 0.1 to 5.6 $m^2\ m^{-2}$ during the field campaign window. A high correlation coefficient (0.94) and low error (RMSE $= 0.74\ m^2\ m^{-2}$) are noted. Similar sensitivity of the estimated LAI (using VV-HV polarizations combined) with in situ measurement was reported for corn in Hosseini et al. (2015), using RADARSAT-2 data. The larger variations in the estimation of PAI above 4.1 $m^2\ m^{-2}$ (i.e., during the tasseling of corn) may be due to increased randomness in the canopy.

3.2.2 Validation of wet biomass

Estimates of wet biomass are shown in Fig. 16.4. The in situ measurement of wet biomass for wheat ranges from 0.4 to 4.8 $kg\ m^{-2}$ throughout crop development. We obtain a high correlation coefficient ($r = 0.92$) with an RMSE of 0.52 $kg\ m^{-2}$, which is lower

than the PAI evaluation errors. However, the boundary of estimation is spread (0.9 kg m^{-2}) across the 1:1 line when wet biomass exceeds 2.5 kg m^{-2}. Hosseini and McNairn (2017) also summarized such results when estimating wheat total biomass using VV and HV channels.

The behavior of wet biomass estimates (Fig. 16.4) of soybean results in a high correlation coefficient (r = 0.88) and low RMSE of 0.29 kg m^{-2}. Early in the season, soybean biomass is low. An overestimation of PAI was observed during the leaf development stage. Early in development, the soybean canopy closure is very low (PAI < 1.48 m^2 m^{-2}) and exposed soil between rows has a greater contribution to backscatter (Wiseman et al., 2014).

The correlation coefficient (r) and RMSE are 0.91 and 0.86 kg m^{-2}, respectively, for canola. The model estimates diverge after the flowering stage, when the measured biomass is >4.0 kg m^{-2}. The sensitivity of radar backscatter to the accumulation of canola biomass throughout leaf development to the flowering stage is likely. At later growth stages, we also observed saturation of the C-band effect on estimates. In contrast to PAI, the overall estimation is marginally better in the case of wet biomass predictions.

The in situ measured wet biomass of oats varies from 0.076 to 5.5 kg m^{-2}. In contrast, the estimates range from 0.05 to 4.0 kg m^{-2}. The r is 0.95 for wet biomass with an RMSE of 0.54 kg m^{-2}. The wet biomass estimates follow the 1:1 line better than PAI. The wet biomass estimates of corn follow the 1:1 line (Fig. 16.4) with r = 0.87 and an RMSE of 1.01 kg m^{-2}. Despite this, the deviation in wet biomass estimations is comparatively higher as plants advance to the tasseling stage.

3.3 Generation of plant area index and wet biomass maps using GEE4Bio

The WCM inversion algorithm in GEE is used to produce PAI and biomass maps of the Carman test site with an area of 26 × 48 km^2 using VV and VH backscatter intensities for Sentinel-1 acquisitions on three dates. High-resolution (20-m) PAI and biomass maps for the three acquisition dates are shown in Figs. 16.5 and 16.6. Both the spatial and temporal variability in plant growth are noted in these inventory maps. The GEE4Bio processing chain takes about 40 s to derive these inventory maps from a single acquisition of Sentinel-1.

The ground data indicate that most of the wheat and oat fields were at tillering through the second week of June, with a mean wet biomass of 1.02 kg m^{-2} and PAI of 3.44 m^2 m^{-2}. Similar results are evident from Figs. 16.5 and 16.6. On the other hand, soybean seeding was completed through this period, and the plants were in their unifoliate to third trifoliate phenology stage (Agriculture, 2016). Therefore, the biophysical parameter maps derived from the Jun. 13 image indicate very low PAI and biomass levels.

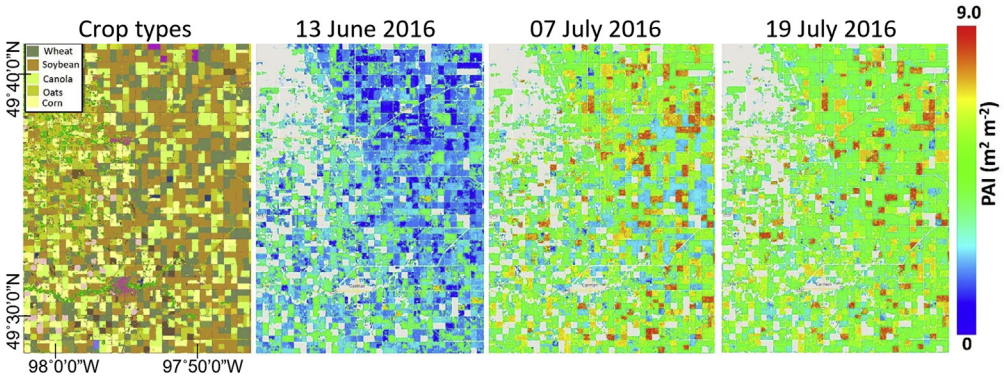

Figure 16.5 Plant area index (PAI) ($m^2\ m^{-2}$) inventory maps over the test site for different acquisitions of Sentinel-1. Other land cover classes are masked on the inventory maps.

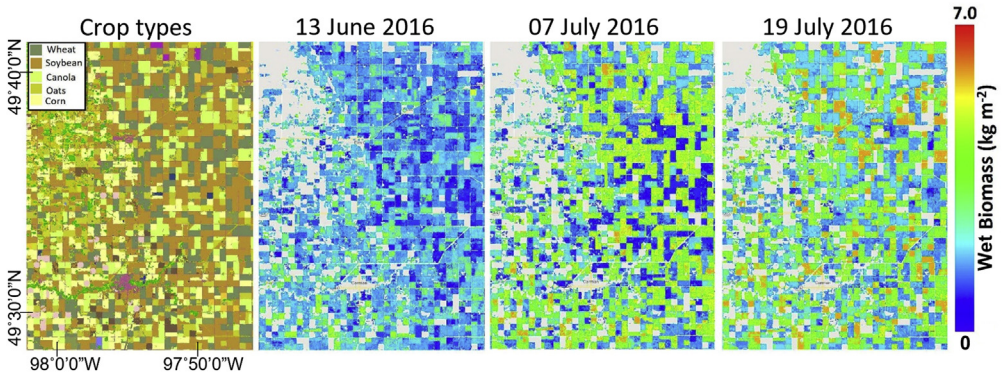

Figure 16.6 Wet biomass (kg m^{-2}) inventory maps over the test site for different acquisitions of Sentinel-1. Other land cover classes are masked on the inventory maps.

The PAI and wet biomass estimates in most of the canola fields indicated low values ($0.7\ m^2\ m^{-2}$ and $0.5\ kg\ m^{-2}$) compared with the cereal crops on June 13. During this period, canola plants were in the emergent to early rosette growth state, which affects the soil contribution, primarily radar backscatter. A similar effect of soil components (surface roughness and moisture content) is well-explained during the early phase of crop development when vegetation cover is low over the soil surface (Baghdadi et al., 2017). However, temporal changes in surface roughness are moderate after the plant starts vegetative growth. Except for specific cultivation practices (harrowing or tillage) or a heavy rainfall event, roughness seldom changes during the early seeding time.

Most cornfields were in their primary vegetative stage during the second week of June, and the average PAI and wet biomass was $0.36\ m^2\ m^{-2}$ and $0.3\ kg\ m^{-2}$,

respectively. However, the PAI and wet biomass maps overestimate both the PAI and wet biomass by 0.5 $m^2\ m^{-2}$ and 0.7 $kg\ m^{-2}$, respectively. These outcomes agree with the validation results presented in Figs. 16.3 and 16.4. This overestimation is likely due to the low cropping density of corn plants and the significant effect of the soil component.

The inventory maps for succeeding acquisition dates indicate an increase in both the PAI and wet biomass values of all crops. Rapid growth is evident in canola with an increased PAI and wet biomass up to 5.7 $m^2\ m^{-2}$ and 4.2 $kg\ m^{-2}$, respectively. For corn, the average growth was observed with a PAI and wet biomass of 4.1 $m^2\ m^{-2}$ and 3.5 $kg\ m^{-2}$, respectively. During the third week of July, we observe pick values of PAI and wet biomass irrespective of the crop types, as they advanced to the end of their vegetative growth (Agriculture, 2016).

4. Conclusion

This chapter demonstrates a unified processing chain for end-users to estimate PAI and wet biomass exploiting Sentinel-1 GRD data on the GEE platform. The RFR model is used in this framework for inversion of the WCM. In this cloud computing framework, applicability of the RFR-based inversion method is evaluated for five major crops using Sentinel-1 dual-pol (VV and VH) SAR data. The crop inventory maps showcased the potential by capturing spatial variability between crop fields over the growing period, leveraging production estimates.

To go from scientific applications to operational monitoring, the proposed processing chain, named GEE4Bio, needs to be rigorously tested with more crop types for application to a wider range of cropping systems. A goal of the JECAM SAR Inter-Comparison Experiment is to gather data from regional test sites and diverse cropping systems. This experiment would benefit from the efficiency of a GEE cloud computing platform. Moreover, this representation of a cloud-based framework produces insights into possible prototypes for managing high volumes of data, as anticipated from planned operational SAR missions. The results presented here demonstrate the usefulness of GEE for regional biophysical parameter retrieval. Such an approach could significantly advance the operational use of SAR for agricultural monitoring.

Acknowledgments

The authors would like to thank the ground team members for data collection through the SMAPVEX16-MB campaign, and the European Space Agency for providing Sentinel-1 through the Copernicus Open Access Hub. Also, authors acknowledge the GEO-AWS Earth Observation Cloud Credits Program, which provided a testbed for cloud computation through the project: "AWS4AgriSAR-Crop inventory mapping from SAR data on the cloud computing platform." This research was supported in part by the Shastri Indo-Canadian Institute, India.

Code availability

Extract by points code in GEE. https://code.earthengine.google.com/d767149c290192a0b175385e62bea544.

GEE code for mapping. https://code.earthengine.google.com/32e06a03325faa2e6720e11af0e58ad2.

Google Colab ipynb link. https://colab.research.google.com/drive/1UGQuSZHuZplZfUKJoPVAVvrple-YQcAM?usp=sharing.

References

Agriculture, M.B., 2016. Agriculture—Province of Manitoba. http://www.gov.mb.ca/agriculture/crops/seasonal-reports/crop-report-archive/index.html.

Ali, I., Naeimi, V., Cao, S., Elefante, S., Bauer-Marschallinger, B., Wagner, W., 2017. Sentinel-1 data cube exploitation: tools, products, services and quality control. Proc. Big Data Space 40–43.

Attema, E., Ulaby, F.T., 1978. Vegetation modeled as a water cloud. Radio Sci. 13 (2), 357–364.

Baghdadi, N., El Hajj, M., Zribi, M., Bousbih, S., 2017. Calibration of the water cloud model at C-Band for winter crop fields and grasslands. Rem. Sens. 9 (9), 969.

Baruth, B., Royer, A., Klisch, A., Genovese, G., 2008. The use of remote sensing within the MARS crop yield monitoring system of the European Commission. Int. Arch. Photogram. Rem. Sens. Spatial Inf. Sci. 37, 935–940.

Bériaux, E., Lambot, S., Defourny, P., 2011. Estimating surface-soil moisture for retrieving maize leaf-area index from SAR data. Can. J. Rem. Sens. 37 (1), 136–150.

Bériaux, E., Waldner, F., Collienne, F., Bogaert, P., Defourny, P., 2015. Maize leaf area index retrieval from synthetic quad pol SAR time series using the water cloud model. Rem. Sens. 7 (12), 16204–16225.

Bhuiyan, H.A., McNairn, H., Powers, J., Friesen, M., Pacheco, A., Jack- son, T.J., Cosh, M.H., Colliander, A., Berg, A., Rowlandson, T., et al., 2018. Assessing SMAP soil moisture scaling and retrieval in the Carman (Canada) study site. Vadose Zone J. 17 (1). https://doi.org/10.2136/vzj2018.07.0132.

Bleiholder, H., Weber, E., Lancashire, P., Feller, C., Buhr, L., Hess, M., Wicke, H., Hack, H., Meier, U., Klose, R., et al., 2001. Growth Stages of Mono-and Dicotyledonous Plants, BBCH Monograph. Federal Biological Research Centre for Agriculture and Forestry, Berlin/Braunschweig, Germany, p. 158.

Breiman, L., 2001. Random forests. Mach. Learn. 45 (1), 5–32.

Campos-Taberner, M., Moreno-Martínez, A.́., García-Haro, F., Camps-Valls, G., Robinson, N., Kattge, J., Running, S., 2018. Global estimation of biophysical variables from Google earth engine platform. Rem. Sens. 10 (8), 1167.

Chakraborty, M., Manjunath, K., Panigrahy, S., Kundu, N., Parihar, J., 2005. Rice crop parameter retrieval using multi-temporal, multi-incidence angle Radarsat SAR data. ISPRS J. Photogrammetry Remote Sens. 59 (5), 310–322.

Chauhan, S., Srivastava, H.S., Patel, P., 2018. Wheat crop biophysical parameters retrieval using hybrid-polarized RISAT-1 SAR data. Remote Sens. Environ. 216, 28–43.

Chipanshi, A., Zhang, Y., Kouadio, L., Newlands, N., Davidson, A., Hill, H., Warren, R., Qian, B., Daneshfar, B., Bedard, F., et al., 2015. Evaluation of the Integrated Canadian Crop Yield Forecaster (ICCYF) model for in- season prediction of crop yield across the Canadian agricultural landscape. Agric. For. Meteorol. 206, 137–150.

Cloude, S.R., Pottier, E., 1996. A review of target decomposition theorems in radar polarimetry. IEEE Trans. Geosci. Remote Sens. 34 (2), 498–518.

Dabrowska-Zielinska, K., Inoue, Y., Kowalik, W., Gruszczynska, M., 2007. Inferring the effect of plant and soil variables on C-and L-band SAR backscatter over agricultural fields, based on model analysis. Adv. Space Res. 39 (1), 139–148.

Davidson, A., Fisette, T., Mcnairn, H., Daneshfar, B., 2017. Detailed crop mapping using remote sensing data (crop data layers). In: Handbook on Remote Sensing for Agricultural Statistics.

Defourny, P., Bontemps, S., Bellemans, N., Cara, C., Dedieu, G., Guzzonato, E., Hagolle, O., Inglada, J., Nicola, L., Rabaute, T., et al., 2019. Near real- time agriculture monitoring at national scale at parcel resolution: performance assessment of the Sen2-Agri automated system in various cropping systems around the world. Remote Sens. Environ. 221, 551–568.

ESA, 2015. User Guides - Sentinel-1 SAR. https://sentinel.esa.int/web/sentinel/user-guides/sentinel-1-sar/acquisition-modes/interferometric-wide-swath.

Fieuzal, R., Baup, F., 2016. Estimation of leaf area index and crop height of sunflowers using multi-temporal optical and SAR satellite data. Int. J. Rem. Sens. 37 (12), 2780–2809.

Fritz, S., See, L., Bayas, J.C.L., Waldner, F., Jacques, D., Becker-Reshef, I., Whitcraft, A., Baruth, B., Bonifacio, R., Crutchfield, J., et al., 2019. A comparison of global agricultural monitoring systems and current gaps. Agric. Syst. 168, 258–272.

Geoglam, 2012. The Ad Hoc Working Group on GEOGLAM. http://ceos.org/ourwork/ad-hoc-teams/geoglam/.

Gorelick, N., Hancher, M., Dixon, M., Ilyushchenko, S., Thau, D., Moore, R., 2017. Google earth engine: planetary-scale geospatial analysis for everyone. Remote Sens. Environ. 202, 18–27.

Graham, A., Harris, R., 2003. Extracting biophysical parameters from remotely sensed radar data: a review of the water cloud model. Prog. Phys. Geogr. 27 (2), 217–229.

Hosseini, M., McNairn, H., 2017. Using multi-polarization C-and L-band syn- thetic aperture radar to estimate biomass and soil moisture of wheat fields. Int. J. Appl. Earth Obs. Geoinf. 58, 50–64.

Hosseini, M., McNairn, H., Merzouki, A., Pacheco, A., 2015. Estimation of Leaf Area Index (LAI) in corn and soybeans using multi-polarization C-and L-band radar data. Remote Sens. Environ. 170, 77–89.

Hoyos-Rivera, G.J., Gomes, R., Willrich, R., Courtiat, J.-P., 2006. Colab: a new paradigm and tool for collaboratively browsing the web. IEEE Trans. Syst. Man Cybern. Syst. Hum. 36 (6), 1074–1085.

Inoue, Y., Sakaiya, E., Wang, C., 2014. Capability of C-band backscattering coefficients from high-resolution satellite SAR sensors to assess biophysical variables in paddy rice. Remote Sens. Environ. 140, 257–266.

Khamala, E., et al., 2017. Review of the Available Remote Sensing Tools, Products, Methodologies and Data to Improve Crop Production Forecasts. http://www.fao.org/3/a-i7569e.pdf.

Liaw, A., Wiener, M., 2002. Classification and regression by random forest. R. News 2 (3), 18–22.

Lievens, H., Verhoest, N.E., 2011. On the retrieval of soil moisture in wheat fields from L-band SAR based on water cloud modeling, the IEM, and effective roughness parameters. Geosci. Rem. Sens. Lett. IEEE 8 (4), 740–744.

Lobell, D.B., Thau, D., Seifert, C., Engle, E., Little, B., 2015. A scalable satellite-based crop yield mapper. Remote Sens. Environ. 164, 324–333.

Mandal, D., Hosseini, M., McNairn, H., Kumar, V., Bhattacharya, A., Rao, Y., Mitchell, S., Robertson, L.D., Davidson, A., Dabrowska-Zielinska, K., 2019a. An investigation of inversion methodologies to retrieve the leaf area index of corn from C-band SAR data. Int. J. Appl. Earth Obs. Geoinf. 82, 101893.

Mandal, D., Kumar, V., McNairn, H., Bhattacharya, A., Rao, Y., 2019b. Joint estimation of plant area index (PAI) and wet biomass in wheat and soybean from C-band polarimetric SAR data. Int. J. Appl. Earth Observ. Geoinform. 79, 24–34.

Mandal, D., Kumar, V., Bhattacharya, A., Rao, Y.S., Siqueira, P., Bera, S., 2018. Sen4Rice: a processing chain for differentiating early and late transplanted rice using time-series sentinel-1 SAR data with Google earth engine. Geosci. Rem. Sens. Lett. IEEE 15 (12), 1947–1951. https://doi.org/10.1109/LGRS.2018.2865816.

Mandal, D., Bhattacharya, A., Rao, Y.S., 2021. Radar Remote Sensing for Crop Biophysical Parameter Estimation. Springer Singapore.

Mattia, F., Satalino, G., Balenzano, A., Rinaldi, M., Steduto, P., Moreno, J., 2015. Sentinel-1 for wheat mapping and soil moisture retrieval. In: Geoscience and Remote Sensing Symposium (IGARSS), 2015 IEEE International. IEEE, pp. 2832–2835.

McNairn, H., Hochheim, K., Rabe, N., 2004. Applying polarimetric radar imagery for mapping the productivity of wheat crops. Can. J. Rem. Sens. 30 (3), 517–524.

McNairn, H., Tom, J.J., Powers, J., Bélair, S., Berg, A., Bullock, P., Colliander, A., Cosh, M.H., Kim, S.-B., Ramata, M., Pacheco, A., Merzouki, A., 2016. Experimental Plan SMAP Validation Experiment 2016 in Mani- Toba, Canada (SMAPVEX16-MB). https://smap.jpl.nasa.gov/internal_resources/390.

Moŕe, J.J., 1978. The Levenberg-Marquardt algorithm: implementation and theory. In: Numerical Analysis. Springer, pp. 105–116.
Mulla, D.J., 2013. Twenty five years of remote sensing in precision agriculture: key advances and remaining knowledge gaps. Biosyst. Eng. 114 (4), 358–371.
NISAR Science Team, 2018. NASA-ISRO SAR (NISAR) Mission Science Users' Handbook. Tech. rep. Jet Propulsion Laboratory, California Institute of Technology. https://nisar.jpl.nasa.gov/files/nisar/NISAR_Science_Users_Handbook.pdf.
Parihar, J.S., Oza, M.P., 2006. FASAL: an integrated approach for crop assessment and production forecasting. In: Agriculture and Hydrology Applications of Remote Sensing, vol. 6411. International Society for Optics and Photonics, p. 641101.
Prevot, L., Champion, I., Guyot, G., 1993. Estimating surface soil moisture and leaf area index of a wheat canopy using a dual-frequency (C and X bands) scatterometer. Remote Sens. Environ. 46 (3), 331–339.
Robertson, L.D., Davidson, A., McNairn, H., Hosseini, M., Mitchell, S., de Abelleyra, D., Verón, S., Cosh, M.H., July 2018. Sar speckle filtering and agriculture field size: development of SAR data processing best practices for the JECAM SAR Inter-Comparison Experiment. In: IGARSS 2018 - 2018 IEEE International Geoscience and Remote Sensing Symposium, pp. 3828–3831.
Shelestov, A., Lavreniuk, M., Kussul, N., Novikov, A., Skakun, S., 2017. Exploring Google earth engine platform for Big Data Processing: classification of multi-temporal satellite imagery for crop mapping. Front. Earth Sci. 5, 17.
Steele-Dunne, S.C., McNairn, H., Monsivais-Huertero, A., Judge, J., Liu, P., Papathanassiou, K., 2017. Radar remote sensing of agricultural canopies: a review. IEEE J. Sel. Top. Appl. Earth Obs. Rem. Sens. 10 (5), 2249–2273.
Torbick, N., Chowdhury, D., Salas, W., Qi, J., 2017. Monitoring rice agri- culture across Myanmar using time series Sentinel-1 assisted by Landsat-8 and PALSAR-2. Rem. Sens. 9 (2), 119.
Verrelst, J., Muñoz, J., Alonso, L., Delegido, J., Rivera, J.P., Camps-Valls, G., Moreno, J., 2012. Machine learning regression algorithms for biophysical parameter retrieval: opportunities for Sentinel-2 and-3. Remote Sens. Environ. 118, 127–139.
Wagner, W., 2015. Big data infrastructures for processing sentinel data. In: Photogrammetric Week, vol. 15, pp. 93–104.
Whitcraft, A.K., Becker-Reshef, I., Justice, C.O., Gifford, L., Kavvada, A., Jarvis, I., 2019. No pixel left behind: toward integrating earth observations for agriculture into the United Nations Sustainable development goals framework. Remote Sens. Environ. 235, 111470.
Wiseman, G., McNairn, H., Homayouni, S., Shang, J., 2014. RADARSAT- 2 polarimetric SAR response to crop biomass for agricultural production monitoring. IEEE J. Sel. Top. Appl. Earth Obs. Rem. Sens. 7 (11), 4461–4471.
Wu, B., Meng, J., Li, Q., Yan, N., Du, X., Zhang, M., 2014. Remote sensing- based global crop monitoring: experiences with China's CropWatch system. Int. J. Digital Earth 7 (2), 113–137.
Xiong, J., Thenkabail, P.S., Gumma, M.K., Teluguntla, P., Poehnelt, J., Congalton, R.G., Yadav, K., Thau, D., 2017. Automated cropland map- ping of continental Africa using Google Earth Engine cloud computing. ISPRS J. Photogrammetry Remote Sens. 126, 225–244.